MATERIALS SCIENCE

Oxide-mediated recovery of field-effect mobility in plasma-treated MoS_2

Jakub Jadwiszczak,[1,2,3] Colin O'Callaghan,[1,2,3] Yangbo Zhou,[1,2,3,4] Daniel S. Fox,[1,2,3] Eamonn Weitz,[1] Darragh Keane,[2,3,5] Conor P. Cullen,[2,3,5] Ian O'Reilly,[1] Clive Downing,[2,3] Aleksey Shmeliov,[2,3,5] Pierce Maguire,[1,2,3] John J. Gough,[1,2] Cormac McGuinness,[1,2] Mauro S. Ferreira,[1,2,3] A. Louise Bradley,[1,2] John J. Boland,[2,3,5] Georg S. Duesberg,[2,3,5,6] Valeria Nicolosi,[2,3,5] Hongzhou Zhang[1,2,3]*

Precise tunability of electronic properties of two-dimensional (2D) nanomaterials is a key goal of current research in this field of materials science. Chemical modification of layered transition metal dichalcogenides leads to the creation of heterostructures of low-dimensional variants of these materials. In particular, the effect of oxygen-containing plasma treatment on molybdenum disulfide (MoS_2) has long been thought to be detrimental to the electrical performance of the material. We show that the mobility and conductivity of MoS_2 can be precisely controlled and improved by systematic exposure to oxygen/argon plasma and characterize the material using advanced spectroscopy and microscopy. Through complementary theoretical modeling, which confirms conductivity enhancement, we infer the role of a transient 2D substoichiometric phase of molybdenum trioxide (2D-MoO_x) in modulating the electronic behavior of the material. Deduction of the beneficial role of MoO_x will serve to open the field to new approaches with regard to the tunability of 2D semiconductors by their low-dimensional oxides in nanomodified heterostructures.

INTRODUCTION

The recent decade has produced intense research into layered two-dimensional (2D) nanomaterials, with transition metal dichalcogenides (TMDs), such as MoS_2, being the prime focus in the area of novel nanoelectronics (*1*–*5*). Progress demands that a nanofabrication methodology is developed to control the structure and properties of semiconducting layered crystals so that desired functionalities are obtained for these materials in the future. These may include phase transitions (*6*, *7*) or conductivity modulation for next-generation data storage (*8*, *9*). In particular, the interaction of low-energy radio frequency–generated plasma ions with MoS_2 has already led to the creation of a multitude of devices, including rectifying diodes, photovoltaics, and nonvolatile memories (*10*–*12*). Plasma power and exposure time have emerged as key variables to delineate between chemical etching and physical sputtering regimes (*13*–*16*). Treatment with oxygen-containing plasma leads to the formation of molybdenum trioxide (MoO_3) centers, which have been reported to increase the resistivity of the material and inhibit carrier transport, while retaining relative structural integrity of the now oxide-containing MoS_2 heterostructure (*17*, *18*). Here, we demonstrate the tuning of electrical resistivity of few-layer MoS_2 by treatment with O_2/Ar (1:3) plasma. The field-effect mobility, μ_{FE}, of the MoS_2 channel is seen to deteriorate initially but recovers to above-original levels after 6 s of exposure to the plasma. The associated electrical conductivity of the device is noted to increase by an order of magnitude at this stage. Upon further treatment, the conductivity and mobility drop again and no subsequent recovery is seen. In the limited literature regarding this phenomenon, the reason for the apparent recovery remains under debate (*19*–*21*). Although other means of doping MoS_2 have recently facilitated mobility improvement (*22*, *23*), a molybdenum oxide–mediated n-type doping scheme has not yet been demonstrated. Here, we propose a mechanism of impurity-mediated electrical tuning facilitated by a 2D phase of MoO_x, with advanced spectroscopic and microscopic studies to support electrical characterization. We infer the presence of this substoichiometric 2D molybdenum trioxide phase, which serves to screen charges associated with plasma-created sulfur vacancies (SVs), enhancing mobility in underlying MoS_2 layers after 6 s of plasma treatment, which increases the channel conductivity. Complementary mathematical modeling of conductive networks reveals the beneficial effect of the freshly incorporated oxide in the MoS_2 matrix. Recent theoretical work has predicted the 2D phase of MoO_3 to be a material with a distinctly high acoustic phonon-limited carrier mobility (>3000 $cm^2 V^{-1} s^{-1}$) (*24*), whereas experimental 2D field-effect transistors (FETs) made of substoichiometric exfoliated MoO_3 have reported mobilities far exceeding those of MoS_2 (>1100 $cm^2 V^{-1} s^{-1}$) (*25*, *26*). The advantageous effect of the 2D phase of MoO_x on the electrical properties of MoS_2 may play a key role in the applications of planar heterostructures of layered TMDs in novel electronic devices. Future research into this area must consider the benefits of defect-mediated transport in 2D nanoelectronics.

RESULTS AND DISCUSSION

Recovery of field-effect mobility in plasma-treated MoS_2

For the initial plasma exposures, the level of drain-source current for a four-layer (4L) device varies slightly up until 6 s, when a significant rise in output current is noted, indicating an increase in the conductivity of the channel (Fig. 1A). Subsequent exposures cause a continuing drop in current level until the noise floor of the instrument (10^{-11} A) is reached after 12 s of plasma treatment (for a closer analysis of device stability, see fig. S4). The gate characteristics (Fig. 1B) of the n-type

[1]School of Physics, Trinity College Dublin, Dublin 2, Ireland. [2]Centre for Research on Adaptive Nanostructures and Nanodevices, Trinity College Dublin, Dublin 2, Ireland. [3]Advanced Materials and BioEngineering Research Centre, Trinity College Dublin, Dublin 2, Ireland. [4]School of Materials Science and Engineering, Nanchang University, 999 Xuefu Road, Nanchang, Jiangxi 330031, China. [5]School of Chemistry, Trinity College Dublin, Dublin 2, Ireland. [6]Institute of Physics, EIT 2, Faculty of Electrical Engineering and Information Technology, Universität der Bundeswehr München, Werner-Heisenberg-Weg 39, 85577 Neubiberg, Germany.
*Corresponding author. Email: hozhang@tcd.ie

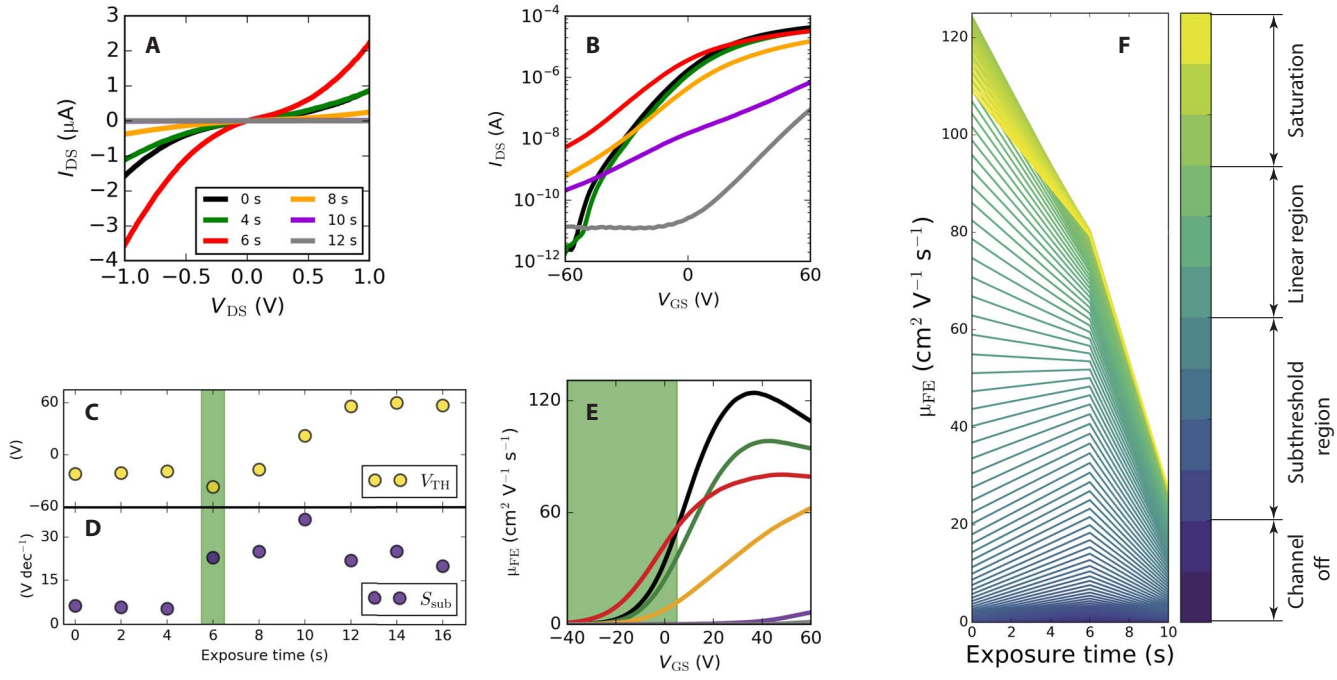

Fig. 1. Characterization of the 4L device. Note that (A), (B), and (E) share the same color legend and that all measurements were performed at room temperature. (**A**) *I-V* curve evolution over exposure time. All curves are measured at zero gate bias. We note the increased current density observed after 6 s (red). (**B**) Gate sweeps of the same device over exposure time. The curves after 6, 8, and 10 s show a largely linear response in the semi-log plot at low gate biases and do not reach threshold over standard sweep range. Subsequent treatment until 12 s drastically shifts V_{TH} to positive gate biases and lowers the current by several orders of magnitude. (**C**) Threshold voltage for the same device shows a sudden drop at 6 s followed by a steady increase to extremely positive gate biases over treatment time. (**D**) Subthreshold swing variation with exposure time shows a diminished response to the gate field starting at 6 s. The area marked in green in (C) and (D) indicates the electrical recovery region. (**E**) Extraction of field-effect mobility for the same 4L device across the whole gate bias range (graph begins from −40 V for clarity). The peak mobility reached in the curves is seen to degrade over time. The green region marks the area of the gate sweep where the 6-s exposure attains highest relative mobility values (red curve). (**F**) Mobility change over plasma treatment time extracted at gate biases between −60 and 60 V. The color legend explicitly maps the curves onto different regions of the gate sweep. The increase at 6 s is visualized in the form of rising recovery peaks in the body of the plot, which correspond to 6-s mobilities evaluated in the green area marked in (E).

MoS_2 change significantly after 6 s. The level of output current at negative gate values increases by several orders of magnitude at 6 s, implying a drastic shift in the threshold voltage (V_{TH}) to negative gate biases. Correlated with this is the change in the sensitivity of the output current to the applied gate-source bias (V_{GS}), with a much more gradual increase in output current throughout the sweep. Figure 1 (C and D) tracks the evolution of the threshold gate voltage (V_{TH}) and the subthreshold swing (S_{sub}) over plasma exposure time. The threshold voltage is seen to shift from ≈−21 V for the untreated device to ≈−37 V at 6 s of exposure and subsequently to large positive gate biases after 10 s. The shift toward negative threshold voltages at 6 s implies increased depletion mode functionality for n-type devices, whereas the upshift of V_{TH} after further exposure denotes an increase of p-type doping. S_{sub}, in turn, initially shows little change until it increases fivefold at 6 s and up to eightfold at 10 s relative to the values before treatment. Upon further exposure, it drops again to ≈25 volts per decade as V_{TH} is shifted to large positive gate biases. At 6 s, the sample shows a marked increase in S_{sub}, indicating that it is less sensitive to variations in the gate field around the region where the FET conductive channel is formed. This is expected to occur if the now-doped few topmost layers of the device have an increased charge trap density (*22*), originating from the plasma treatment.

The field-effect mobility, μ_{FE}, of the device is plotted as a function of gate bias in Fig. 1E. The peak value of mobility is seen to drop with exposure time, and the gate bias necessary to reach saturation shifts toward larger V_{GS}. For V_{GS} in the region from −40 to 5 V (highlighted green area in the plot), the mobility at 6 s can now be tuned to much higher values than for the untreated device, with the corresponding conductance of the device increasing by more than one order of magnitude in this region. Subsequent treatments at 8 and 10 s decrease μ_{FE} markedly, and no recovery is seen beyond this point. In addition, the change in μ_{FE} over exposure time at each applied gate bias between −60 and 60 V is charted in Fig. 1F in one-volt steps. The extracted curves are color-mapped to the palette seen on the right, scaling from extremely low (−60 V) to extremely high (60 V) gate biases. Inside the decay envelope of the peak mobility evident from the edge contour of this graph, we observe a series of recovery peaks around the region corresponding to a treatment time of 6 s. This recovery is pronounced in the linear regime near V_{TH} (that is, where μ_{FE} rises above initial values extracted for the untreated device). This corresponds directly to the green region in Fig. 1E, where the red curve (6 s) attains higher values than the other curves, that is, across $V_{GS} \in [-60\ V, 5\ V]$. The subsequent drop in μ_{FE} and conductance is a direct consequence of material etching and introduction of scattering centers that happens after 10 s.

The notable increase in current density seen in Fig. 1A; the close-to-linear response to the variation in gate bias at 6, 8, and 10 s (red, orange, and purple curves in Fig. 1B, respectively); and the increase in S_{sub} all hint at the presence of a highly conductive phase in the

material comprising the FET channel at 6 s of exposure, which is responsible for the recovery. In the following sections, we go on to infer that this phase is a 2D form of MoO_x produced by a chemical reaction with the plasma. To highlight the role of oxygen in electrical tuning, we repeated the experiment using pure Ar plasma and did not observe a recovery (figs. S9 and S10). Note that modulation of the Schottky interface between the sample and the contacts is not responsible for the noted μ_{FE} increase. As the electrodes are deposited on untreated MoS_2 as effective top contacts, the interface is protected from plasma exposure throughout the experiments. This is in contrast to a reported study where the Schottky barrier height between the MoS_2 and electrode metal can be modulated by pretreating the MoS_2 with oxygen-containing plasma before contact deposition (*27*). Because the chemical modification is confined to the sample surface, we proceed to investigate the structural and chemical change to the topmost layer of the MoS_2 in the following sections.

MoS_2 surface modification by oxygen insertion

We use atomic force microscopy (AFM) to track the thickness variation and surface roughness of the plasma-treated flake. Phase maps of the same region on a 4L flake are shown in Fig. 2 (A to C), with notable change in contrast indicating material difference over time. Figure 2D charts the change in the edge heights evaluated from line profiles across the edges of the 4L and 5L regions (fig. S11). The initial edge height on the 4L portion increases by ≈30% from 0 to 6 s and that on the 5L area increases by ≈21%. This is followed by a subsequent drop in height for longer exposure times. This initial insertion agrees well with the expected height change if the top layer of MoS_2 were to be replaced by a layer of α-MoO_3 or MoO_x with edge-sharing octahedra (29% for 4L and 23% for 5L). The surface roughness (Fig. 2E) may show a peak at 6 s owing to the formation of oxide patches, but the average value does not vary more than the thickness of one layer of MoS_2 or MoO_3 in the first 8 s of exposure. The peak in edge height at 6 s is a critical point at which the etching mechanism shifts from one largely dominated by chemical oxygen insertion into the lattice to one where argon-dominated sputtering of material and removal of species from the surface take over. With increasing doses of the plasma, the integration of oxygen into the mechanically exfoliated 2H-MoS_2 structure will introduce considerable change, including the rearrangement of electronic density and effective lattice deformation, which increases the interlayer distance. Oxygen intercalation between the top layer and the rest of the stack may also occur (*28*). All these factors lead to a rise in the thickness of the thin $MoS_{2-x}O_x$ film (*14*, *28*–*31*) and can lead to rupturing (*32*) while forming oxide-containing patches on the surface at the same time. These fine oxide patches, spectroscopically determined by Ko *et al.* (*33*) to exist, can be seen in the scanning electron micrograph in Fig. 2G (for larger-scale images, see fig. S13). The contrast is due to the higher work function of MoO_3 (6.6 eV) (*34*) compared with that of MoS_2 (≈4.04 to 4.47 eV) (*35*). The structural modification undergone by the MoS_2 in the plasma chamber can also be linked to the change in its optical contrast over time (see discussion in fig. S12). A recent study has shown that substoichiometric MoO_{3-x} can be volatile and even removed by Ar flow at low temperatures (*36*). In the O_2/Ar plasma physical sputtering–dominated regime, the surface roughness is seen to increase by more than 1 nm at 28 s of exposure due to Ar^+-related etching and redeposition of material on the surface (*15*, *16*). However, the unchanging surface roughness up until 8 s indicates initial direct conversion of MoS_2 into a planar oxide. Most importantly, the edge height trend correlates with the electrical recovery discussed in the previous section, with a peak at 6 s.

Spectroscopic analyses of the surface-bound oxide

We investigate the change to the chemical content of our MoS_2 devices by using Raman, photoluminescence (PL), energy-dispersive x-ray (EDX), and x-ray photoelectron (XPS) spectroscopies. The offset Raman spectra of the 4L flake (Fig. 3A) show notable shifts in the characteristic peaks corresponding to the A_{1g} mode at ≈407 cm^{-1} and the E^1_{2g} mode at ≈384.5 cm^{-1} once the sample is exposed to the plasma. After only 2 s of treatment (and accompanied by a decrease in

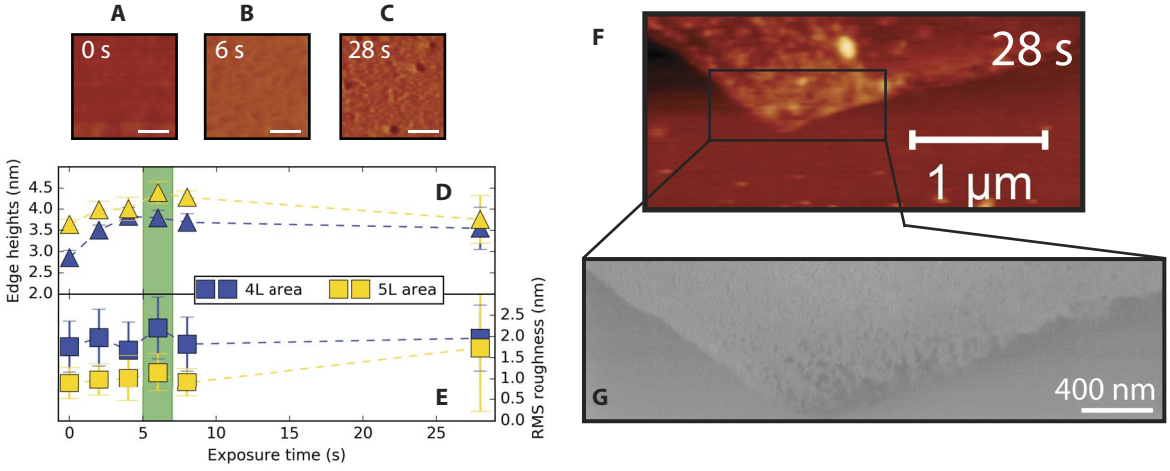

Fig. 2. Surface morphology of plasma-treated MoS_2. (**A** to **C**) Phase maps of the same region of a 4L flake, showing notable material contrast on the surface as oxides are formed over time. Scale bars, 200 nm. (**D**) Chart of edge heights extracted along line profiles after each exposure time (see all the raw height maps in fig. S11). The region in green is the edge height peak, which correlates with the electrical recovery time at 6 s. (**E**) Root mean square (RMS) surface roughness profiles extracted over time from height maps of the 4L and 5L regions of the flake. (**F**) AFM map of bottom edge of this flake after 28 s of plasma etching. Visible voids are seen along the bottom of the sample (**G**) scanning electron microscopy (SEM) image of the corner of the same flake, exhibiting dark contrast pits on the edge, corresponding to oxidized MoS_2 regions.

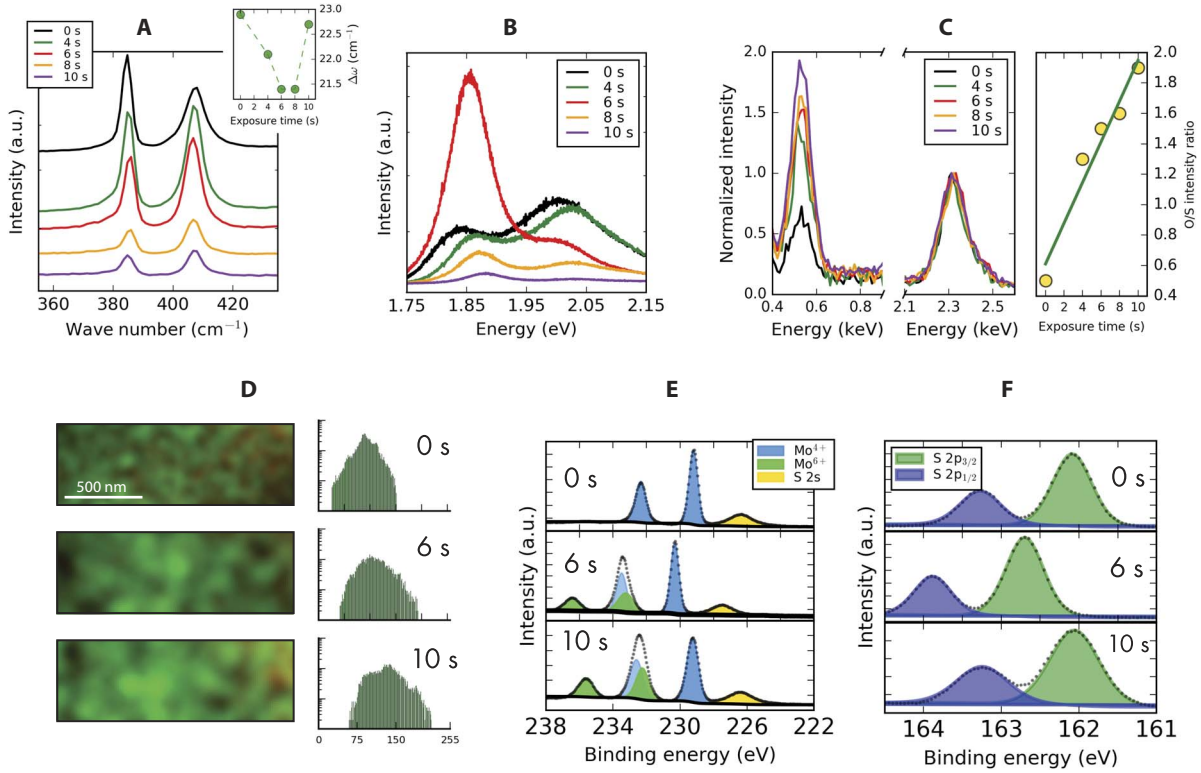

Fig. 3. Spectroscopic signatures of oxidized MoS_2. (**A**) Raman spectrum of 4L MoS_2 over plasma treatment time shown in the semi-log plot. The inset tracks the time evolution of the separation between the E^1_{2g} and A_{1g} peaks. (**B**) PL spectrum of 4L MoS_2 as it changes over plasma exposure time, showing significant A exciton enhancement at 6 s of treatment. au, arbitrary units. (**C**) Left: Time evolution of EDX spectrum normalized to the sulfur-K_α line taken from a suspended 4L flake. Right: Ratio of O/S elemental signal intensity tracked over exposure time. The green line is a linear fit to the data. (**D**) Areal EDX mapping of sulfur (red) and oxygen (green) content in the same 4L sample at 0, 6, and 10 s of plasma treatment. The associated histograms visualize the intensity distribution of the green oxygen pixels in the maps. Scale bar, 500 nm. (**E**) XPS spectra of the Mo 3d region showing increased MoO_3 content overtime. (**F**) S 2p region of the XPS spectrum.

amplitude) the E^1_{2g} peak blueshifts to ≈385 cm^{-1}, whereas the intensity of the A_{1g} peak increases by ~32% and its position upshifts slightly, reducing the fitted peak separation (see inset and fits in fig. S14). As the Raman spectra evolve over time, the peak separation at the recovery time of 6 s narrows, whereas the full width at half maximum (FWHM) of the A_{1g} out-of-plane mode is reduced. Its intensity now rises above that of the in-plane mode and remains as such for longer plasma treatment times, where both intensities are greatly quenched and peaks begin to broaden and separate.

The insertion of oxygen into the MoS_2 crystal lattice by the plasma can account for the change in the dielectric screening environment and the restoring forces between adjacent MoS_2 molecular layers, thereby affecting the frequencies of both characteristic modes. An increase in Δω occurs when MoO_3 replaces MoS_2 on the surface of a MoS_2 monolayer (see 1L data for comparison in fig. S14) (*33*, *37*). Conversely, the peak separation remains constant in the monolayer or is reduced when no oxides are detected after plasma treatment (*7*, *28*, *38*). In addition, the asymmetric peak broadening of both peaks over longer exposure times seen in Fig. 3A has been associated with the presence of additional defect-induced phonons originating from oxide centers in plasma-treated MoS_2 (*33*). The unusual variation in the intensity ratios for this plasma-treated 4L sample may originate in a change to the stacking order of the MoS_2 layers and/or surface reconstructions. If the top layer uncouples from the rest of the MoS_2 lattice, it may affect the on-resonance condition for the Raman scattering in this van der Waals layered system and alter the relative mode ratios (*39*, *40*).

The PL spectra of the 4L sample are presented in Fig. 3B. For the initial exposure times, the luminescence intensity associated with the B exciton at ~2 eV dominates over the A exciton intensity at 1.85 eV, which is characteristic of the indirect-gap nature of nonmonolayer MoS_2. The energy of both peaks is slightly blueshifted after initial plasma exposures and their intensity also drops. With further exposure to the recovery time of 6 s, the direct-gap emission is greatly enhanced by ~120%. Direct emission persists until it is fully quenched at longer exposure times. This anomalous effect noted at 6 s matches well with the picture of the top layer becoming decoupled from the rest of the MoS_2 stack, an effect previously observed and attributed to oxygen intercalation (*28*). Meanwhile, the bidirectional shifts of both peaks over time serve to illustrate band structure distortion induced by the plasma treatment. The PL quenching at longer exposure times is due to the defect-induced midgap states that inhibit direct excitonic recombination (*37*, *41*). The associated quenching rate increases greatly with defect density, inhibiting the radiative recombination completely after 10 s of exposure (see figs. S15 and S16 for monolayer data).

We plot the relationship of the oxygen K_α and sulfur K_α EDX peak intensities to the plasma exposure time derived from the normalized spectra, which we obtained from the same region of a 4L sample after subsequent treatments (Fig. 3C). Oxygen content has increased more than threefold in the first 10 s of exposure to the plasma and changes almost linearly with time. Areas high in O signal also show a reduced S signal, suggesting that the oxygen has replaced the sulfur in the MoS_2 lattice through an oxide-forming chemical reaction (see also figs. S18

and S19 for monolayer data). Areal EDX mapping of the suspended 4L MoS_2 flake (Fig. 3D) suggests the insertion of oxygen into the MoS_2 structure in a patch-like pattern, as previously proposed (*17*, *42*). The associated color histograms visualize the increased oxygen distribution in the sample with plasma time by increasing green pixel count originating from the O elemental signal.

Figure 3E shows XPS spectra of the Mo 3d region, indicating the increased presence of oxide species over exposure time. For the pristine sample, the peaks around 229 and 232 eV correspond to, respectively, the Mo^{4+} $3d_{5/2}$ and Mo^{4+} $3d_{3/2}$ spin-orbit split components. The 6-s spectrum shows a characteristic Mo^{6+} 3d doublet attributed to MoO_3 (*43*). After 10 s of exposure, the intensity of the trioxide-associated doublet increases further, with a significant ratio of the surface now containing MoO_3 (estimated at 30 to 40% from areas of each fitted component). In addition, a thickogram calculation (*44*) reveals that the intensity attenuation of the 10-s spectrum is consistent, within known parameters, with the presence of a bilayer of 2D-MoO_3 (that is, a bulk unit cell of α-MoO_3) on the surface at this exposure time and 61% of the bilayer of 2D-MoO_3 at 6 s (see calculation details in section S3 and Mo 4p, 4s spectra in fig. S22). In addition, the FWHM of the MoO_3-associated doublets increases from the 6-s to the 10-s spectrum, suggesting the surface formation of a more stoichiometrically complete trioxide between 6 and 10 s of plasma treatment (see also the evidence of small peak originating from the S–O bond at 6 s in fig. S21).

Figure 3F demonstrates the S 2p region. Peak broadening is evident with increased plasma exposure time, indicating a change in the chemical order of the surface. Substoichiometric MoS_{2-x} has also been reported to cause the characteristic broadening of the S 2p doublet (*45*), consistent with the picture of sulfur atoms being removed from the surface of the MoS_2 flakes. Most interestingly, both the Mo 3d and S 2p signals are upshifted after 6 s and downshifted after 10 s in these spectra, which have been corrected to the C 1s core line (table S1). It is widely accepted that MoO_3 can induce hole doping and concomitant downshifting of the MoS_2 peaks due to Fermi level realignment (*37*, *42*, *46*, *47*). This is in agreement with our transfer curves, with significant threshold voltage shift to positive gate biases at higher plasma exposure times (Fig. 1C). The upshift at 6 s may thus correlate with the n-type doping observed in the transfer curves in Fig. 1B.

All the above results demonstrate that the plasma-treated MoS_2 undergoes a continuing oxygen insertion and crystal structure distortion. However, the full unit cell of plasma-generated MoO_3 is an insulator (*17*). The electrical recovery at the 6-s mark indicates that an intermediary phase of substoichiometric MoO_3 may exist between the pristine MoS_2 semiconductor and the MoO_3-rich insulator, causing the transient recovery of electrical properties within the exponential decay envelope known from the literature. This observed trend may suggest the formation of a highly conductive form of MoO_x recently reported in the literature (*25*, *26*).

Nanoscale effects of plasma etching at recovery time

Many etching mechanisms, some contradictory, have been proposed for the surface reaction of oxygen-containing plasma with MoS_2 (*33*, *48*, *49*). To investigate the elusive 2D oxide phase, we go on to study the effects of the plasma etching on the nanoscale by aberration-corrected scanning transmission electron microscopy (AC-STEM). Figure 4A shows a region of a bilayer MoS_2 flake after plasma treatment of 6 s (compare to the pristine flake in fig. S27). Notable damage to the MoS_2 lattice occurs at this exposure time (for complementary HRTEM images, see figs. S23 and S24). Regions of MoS_2 material are completely removed in nanometer-sized regions (see mass-thickness contrast STEM images in fig. S26). These pits deepen with increasing plasma doses and eventually become perforations on thinner flakes. This etching phenomenon is seen to nucleate from individual defective sites, spanning only a few nanometers across. Some of these voids are missing a part of the top molecular layer of MoS_2 after 6 s, leaving behind a bare monolayer region underneath (as confirmed by simulation in figs. S30 and S31). Large-scale AC-STEM micrographs are presented in figs. S28 and S29. These images were used to obtain statistics on the dimensions of voids formed by the plasma in the MoS_2 at 6 and 8 s. Figure 4B demonstrates the distributions of the extracted widths and lengths of imaged voids on

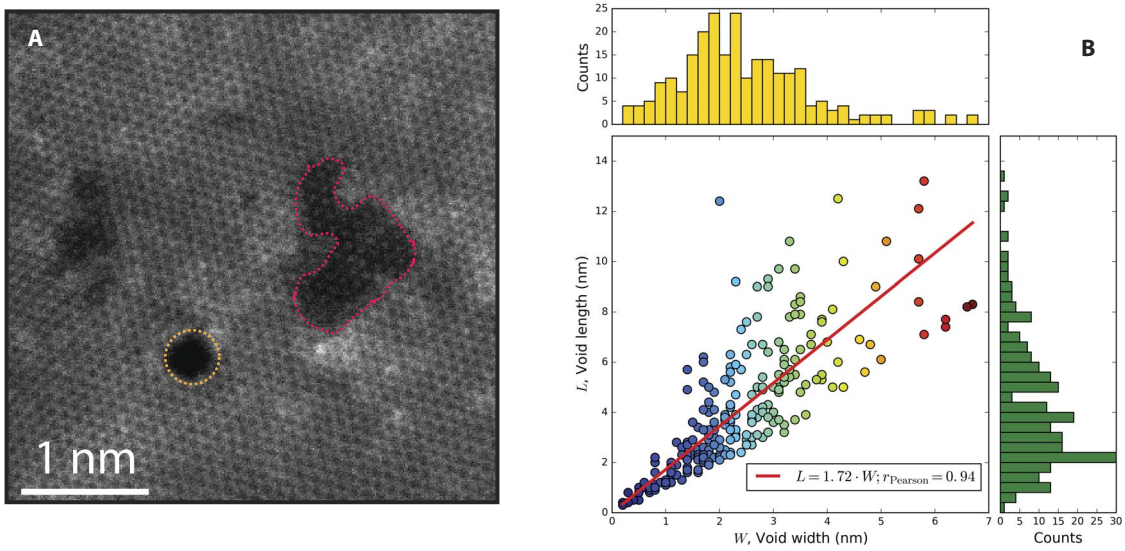

Fig. 4. Evidence of oxide-mediated etching on the nanoscale. (**A**) Typical AC-STEM micrograph showing nanoscale voids forming in bilayer MoS_2 after 6 s of plasma exposure. The region marked in magenta shows an etched pit with part of the top layer missing. The area marked in orange shows a perforation where no material remains. (**B**) Scatterplot and histograms visualizing the distribution of the lateral dimensions of etched voids on this flake after 6 s of plasma exposure. The scatter data are color-mapped from cool to warm with increasing void width.

the bilayer flake. Yellow (green) histograms show the width (length) distributions. Length is here defined as the largest lateral void dimension, whereas width is the dimension perpendicular to it. A positive correlation between the lateral dimensions of the etched voids is extracted from data fitting (see residuals in fig. S32), showing the close-to-isotropic growth of the voids. The average area of a pore at 6 s is 12.5 ± 0.1 nm^2 (see histograms in fig. S33). At this time, the relative total percentage area covered by the voids from images sampled in the AC-STEM is ≈3.6%. The distribution at 8 s is presented in fig. S34.

Markedly, the nanoscale EDX and electron energy-loss spectroscopy (EELS) mapping are performed with the 60 pm electron beam probe return spectra, suggesting very little oxygen presence around the recovery time (see spectra and discussion in fig. S20). It has been demonstrated that oxygen plasma interaction with molybdenum metal leads to the creation of volatile Mo oxides (*50*), whereas a recent study has confirmed oxide volatility in oxidized MoS_2 (*36*). We find that the plasma-formed oxide phase studied presently is volatile under ultrahigh vacuum (UHV). When the sample is left overnight in the in situ testing system (~10^{-6} mbar), the n-type depletion mode functionality is reversed by a drastic shift of V_{TH} toward positive gate biases (see fig. S8 for comparison with UHV-stable insulating MoO_3). Similarly, when inserted into the vacuum chamber of the AC-STEM overnight (~10^{-9} mbar), the freestanding flakes lose their weakly bound surface oxides. The inability to detect oxygen in these atomically resolved voids leads us to infer that the oxide, which was present initially and is responsible for the electrical recovery, was sublimated under UHV conditions, leaving behind the underlying MoS_2 structure.

Dependence of mobility recovery on MoS_2 layer number

To obtain a more informed picture of how the oxide on the top layer of MoS_2 affects the transport behavior of the FET, we fabricated and tested devices of different thicknesses between 1 and 10 layers in the same fashion as the device in Fig. 1. The associated *I-V* curves, gate curves, derived mobilities, and subthreshold swings at each plasma exposure time are all collated in figs. S5 to S7. The highly consistent feature of transfer curves at times when the 2D-MoO_x is present on the top layer is the drastic shift of threshold voltage to negative gate biases. Figure 5A tracks ΔV_{TH} for the tested MoS_2 layer numbers. Here, ΔV_{TH} is defined as the difference between the threshold voltage before treatment and at the point of mobility recovery. For samples of all thicknesses, V_{TH} shifts considerably to negative biases by a similar amount, with the mean shift value of ΔV_{TH} = −19 V marked on the plot by the horizontal yellow line. This behavioral consistency and lack of dependence on layer number indicate the key role of the plasma-modified top surface layer. SVs are known to induce n-type doping and a negative V_{TH} shift in MoS_2 (*51*). Electrons will transfer from MoS_2 to MoO_x to equalize Fermi levels, but the number of electrons transferred (*52*) is $N_e \cong r_m \Delta E/e^2$, where r_m is the mean size of oxide patches at 6 s seen in AC-STEM in Fig. 4A and ΔE is the Fermi energy shift between the oxide and the MoS_2. We calculate values of N_e, which are at least one order of magnitude smaller than the concentration of SVs (the electron concentration being $C_{ox}\,\Delta V_{TH}/e$ ~ 10^{12} cm^{-2}). Hence, V_{TH} will be largely shifted to negative gate biases as plasma-created SVs strongly n-dope the FET channel at the point of recovery. However, at longer plasma times, the oxide patches turn into insulating MoO_3, which act as effective acceptors (*47*). At the same time, the concentration of SVs decreases because they become preferential sites for oxygen incorporation. The vanishing of SVs and the formation of hole-doping MoO_3 eventually cause an imbalance to this interplay, resulting in a positive shift in V_{TH} at longer plasma times (>10 s).

The effect of channel thickness on the screening effect of the metallic patches embedded in the top layer at recovery time can be well understood by tracking the subthreshold swing variation for all the samples over exposure time (fig. S7). In Fig. 5B, we plot the percentage change of S_{sub} for MoS_2 devices of all tested layer thicknesses (that is, a measure of how much S_{sub} increases at recovery time relative to no plasma treatment). The extracted data are well fitted with an asymptotic exponential function (R^2 = 0.99). This demonstrates the critical role that layer thickness plays in allowing the top metallic layer to alter the field effect in the underlying MoS_2 channel. The conductivity of the metallic top layer is not tunable by the back gate (*7*). Hence, the on/off ratio at recovery time is severely reduced for samples of all thicknesses, but this effect is felt more severely by thinner

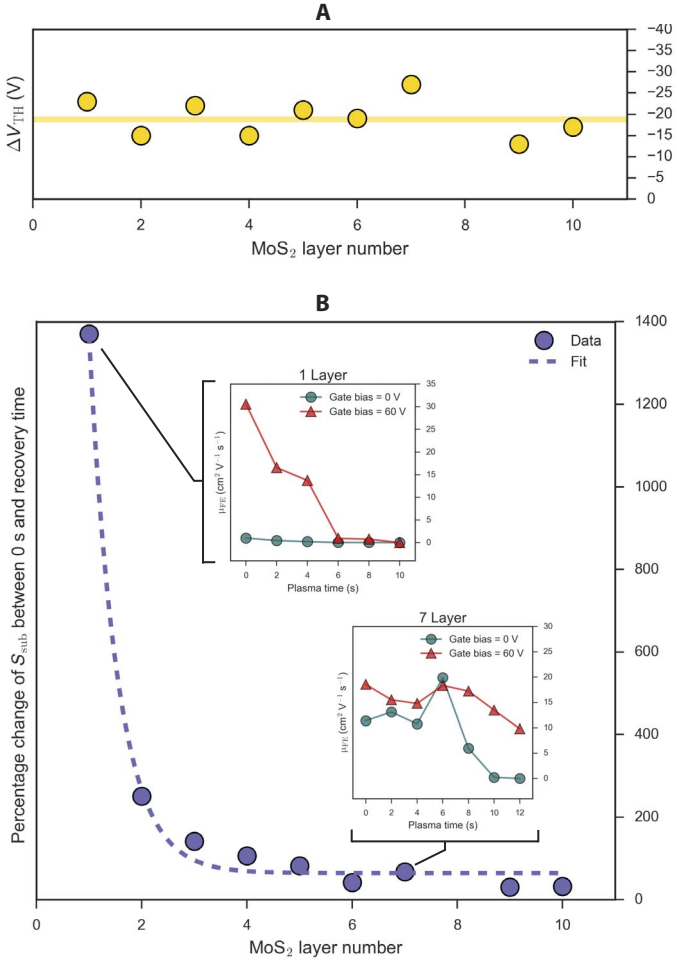

Fig. 5. Effect of layer number on mobility recovery. (**A**) Change in gate threshold voltage between recovery time and pristine MoS_2 tracked as a function of layer number. Devices of all thicknesses show a major V_{TH} shift to negative gate bias at the time of mobility recovery. The mean shift value of −19 V is marked by the horizontal yellow line. (**B**) Percentage increase in subthreshold swing between untreated and recovered stages for samples of all tested thicknesses. S_{sub} increases for all samples at the recovery stage and the effect scales with MoS_2 layer number. Insets track the mobility evolution over exposure time for the 1L and 7L samples in the linear (green) and saturation (red) regimes. The mobility recovery happens for samples thicker than two layers.

samples (hence, much higher S_{sub} values). As thickness of the MoS_2 stack increases, more undamaged semiconducting material is present deeper in the channel, and the screening from the top layer is felt less strongly.

The defect formation from the plasma effectively destroys the 1L and 2L devices (as evidenced by damage to the bilayer in Fig. 4A) before the beneficial effect of the metallic top layer can be experienced by those thin FET channels. The mobility recovery then occurs for thicker samples (>2L) in the linear regime of the transfer curve. This has its origin in (i) the metallic 2D-MoO_x electrostatically shielding the defect-born charged impurity scattering centers in the underlying layers, resulting in enhanced mobility in the below layers of the now-thinned channel, and (ii) the distribution of current across the layers. In the linear regime ($V_{GS} - V_{TH} \approx 0$ V), the centroid of the current distribution is away from the top layers (*53*), with the current mainly conducted in the underlying layers. The metallic 2D-MoO_x effectively screens the surface charges (SVs and other scattering centers) and results in an enhanced mobility in the underlying layers. In the saturation regime, the hot spot moves to the top layers at high gate voltages (*53*). Because the top layer is rich in scattering centers, this has a direct consequence in that the peak mobility in the saturation regime decreases strongly with increasing plasma time. This interplay is illustrated by the insets of μ_{FE} evolution over plasma time for the 1L and 7L samples (representative of thin and thick layer cases). Mobility in the linear regime (green) is does not recover in the 1L case but has a strong recovery peak at 6 s in the 7L case. μ_{FE} recovers thicker than 2L for all samples in the linear regime (fig. S6). The peak mobilities measured at saturation (red) decrease strongly for the 1L case and recover slightly for the 7L case. This again shows that thickness is a key parameter, because the 1L sample is rich in scattering centers, whereas the 7L sample still has pristine MoS_2 layers underneath the screening metallic top layer.

Resistive network modeling of conductivity over time

Modeling of classical conductive networks has proven to be an excellent avenue to describe the global conductive properties of nanoscale devices based on local properties of a network (*54*–*56*). An appropriate conductive network model was thus applied to approximate the effect of ideal plasma-generated chemical conversion on the sheet conductance of single-layer MoS_2. Figure 6A shows a plot of the relative conductance of a simulated MoS_2 network, whose nodes undergo conversion to highly conductive 2D-MoO_x and insulating MoO_3 phases over time (in arbitrary units). The increase in sheet conductance yielded at the start of the simulation qualitatively mirrors the recovery peaks in Fig. 1F. This can only be observed if the conductance of the 2D phase is much higher than that of MoS_2 (see fig. S37 for other cases), and the relative transition rates between phases follow a relationship such that sites that are already defective are more likely to convert (see Materials and Methods). We remark that the nodal phase conversion is abrupt for any given iteration, but the emergent recovery phenomenon experiences a gentle crossover between regimes of different conductance. The relative concentration of conductors that exist in each phase is sampled throughout the simulation and visualized through the color-mapped lattices in (i) to (iv) (see the chart of phase concentrations across iteration steps in fig. S36 of the Supplementary Materials). The sheet conductance rises initially as the concentration of 2D-MoO_x increases. The conductance (and associated field-effect mobility) reaches a peak, just as observed in experimental results in Fig. 1F, and proceeds to drop off because conductors begin to transition to the insulating MoO_3, eventually reaching the insulating stage (for comparison with site destruction, see fig. S38). The differing transition rates affect not only the size of the conductance peak but also the phase concentrations for which it occurs (section S5). The network map sampled at the conductance peak (ii) shows that the spike in sheet conductance occurs with a relative network coverage of 2D-MoO_x at approximately 15%. This differs from the experimentally determined areal void coverage of ≈4% at 6 s but remains well under the site percolation threshold for a square lattice (*57*). The difference may originate in the underestimation of the area of oxide-born defective sites from AC-STEM images of bilayer flakes. Some voids can become filled with adventitious hydrocarbons over time and/or be obscured by a top molecular layer depending on sample orientation when transferring to a TEM grid. This resistive network model demonstrates qualitatively that a highly conductive intermediate oxide phase may serve to facilitate a recovery in the conductance and associated μ_{FE} of a MoS_2 sheet over plasma exposure time.

CONCLUSION AND OUTLOOK

We have demonstrated a simple and reliable method to tune the electronic properties of few-layer MoS_2 FETs by using O_2/Ar (1:3) plasma. The apparent recovery of electrical conductivity is attributed to the temporary presence of a 2D phase of MoO_x, which is formed at some point during 4 and 6 s of plasma exposure. Its effect on the performance of the FET serves to provide a transient recovery of electrical conductivity and carrier mobility, despite the ongoing deformation of the MoS_2 lattice. We have also inferred the existence of this transient 2D oxide phase from evidence collected from advanced spectroscopic and microscopic studies and found that it is unstable under UHV conditions. In addition, we have demonstrated with a robust simulation that the presence of a conductive phase on the surface

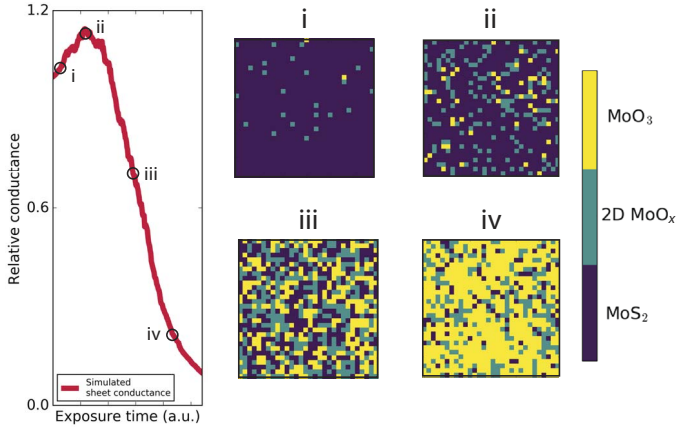

Fig. 6. Resistive network simulation of oxidized MoS_2. Simulated sheet conductance of MoS_2 during the progressive conversion from MoS_2 to 2D-MoO_x to MoO_3. Exposure time, which is expressed in arbitrary units, charts the progress of the plasma-induced chemical oxidation as the simulation is iterated. One site undergoes transformation to the next phase during each iteration. Sites are not destroyed in this simulation, and the plasma-etching process finishes when all sites reach the insulating MoO_3 phase. The distribution of phases in the conductive network at four different iteration stages is shown throughout (i) to (iv), where the subsequent phases are color-mapped to the scale shown on the right. The lattice visualized in (ii) corresponds to the state of the network at the recovery time. The concentration of 2D-MoO_x at that stage is ≈15%.

of MoS_2 may induce a plasma dose-dependent recovery in the conductance of the material network. Our results are of great importance to groups studying novel 2D TMDs and the fundamental properties of their low-dimensional oxides. In addition, the discovery of this phenomenon has broad implications for future van der Waals heterostructure devices and planar circuit architectures. Site-specific plasma modification of MoS_2 can be achieved by polymer protection, creating oxide-rich regions that could operate at negative gate biases and serve as charge storage nodes and/or input valves into further circuit components.

MATERIALS AND METHODS

MoS_2 exfoliation, identification, and transfer

MoS_2 flakes were mechanically exfoliated from commercially available bulk molybdenite crystals (SPI Supplies) using the adhesive tape method and deposited on a precleaned Si substrate capped by 285 nm of SiO_2. Samples were identified through optical contrast measurements and Raman spectroscopy. Electron beam lithography (EBL) was used to define contacts, followed by deposition of metal film (5-nm Ti/35-nm Au) and lift-off in acetone (see optical images of devices in fig. S2). Suspended MoS_2 samples were prepared using the stamp-transfer methodology (*58*) to move flakes from substrates onto TEM grids by etching away the SiO_2 surface underneath a polymer-embedded MoS_2 flake.

Plasma treatment

The on-chip MoS_2 FET devices were modified in a Fischione Instruments 1020 plasma cleaner (see specifications in fig. S1), producing a 13.52-MHz field to ionize a 1:3 mixture of O_2/Ar gas at a constant chamber pressure of ~5 mbar. The samples were always exposed to the plasma for 2 s at a time, at the same position in the chamber (to within ±1 mm), to control the accuracy of the experiment. After each exposure, the samples were removed and characterized electrically.

Electrical measurements

The devices were globally back-gated through the highly doped Si substrate and measured in a two-probe configuration at a pressure of 10^{-4} mbar in the vacuum chamber of a SEM (see sketch of experimental geometry in fig. S3). The source and drain terminals were provided by tungsten nanomanipulator tips (Imina miBot) connecting the deposited contacts to an Agilent B2912A dual-channel sourcemeter.

Microscopy

Samples were prescreened in a Zeiss Ultra microscope in STEM mode at 20 keV to determine appropriate thickness for further TEM and AC-STEM experiments (fig. S25). TEM was carried out in an FEI Titan 80-300 operated at 300 keV at a chamber pressure of 4×10^{-7} mbar. AFM was performed at ambient pressure in an Oxford Asylum system using cantilevers calibrated at 140 kHz. AC-STEM was carried out in a Nion UltraSTEM 200 system operated at 60 keV, at a chamber pressure of ~10^{-9} mbar.

Spectroscopy

Because sampling efficiency from mechanically exfoliated flakes is extremely low, XPS was performed on larger bulk flakes, whose surface (≈2 mm^2) was plasma-treated in the same way as all FET samples after deposition on Si/SiO_2 substrates. The system used a monochromated Al K_α x-ray source with an Omicron EA 125 hemispherical analyzer set to a pass energy of 19 eV, giving a combined instrumental and source resolution of 0.50 eV. The spectra for these samples were fitted with 2H polytype peaks, as is usual for mechanically exfoliated MoS_2 flakes. PL spectroscopy was performed on substrate-supported monolayer flakes using an excitation wavelength of 405 nm. Raman spectroscopy of monolayers was carried out at atmospheric pressure with a HORIBA Jobin Yvon 488-nm laser equipped with 1200 grooves/mm and a charge-coupled device camera. Acquisition time was fixed at 10 acquisitions/s. A 100× objective lens was used. The laser spot size was ≈1 μm, whereas the power of the laser was kept below 1 mW. Raman/PL spectroscopy of 4L flakes was performed with a WITec Alpha 300R microscope using a 532-nm excitation laser, a spectral grating of 1800 lines/mm, and a 100× microscope objective (numerical aperture, 0.95; spot size, ~0.3 μm). Spectra were taken with a laser power of less than 60 μW to minimize heating. EDX mapping was carried out on suspended samples transferred onto TEM grids using the polymer stamp method (see the image in fig. S17) using a Bruker Nano XFlash 5030 detector in a Zeiss Supra SEM at 5 keV, with a step size of 0.7 nm/pixel. Atomically resolved EELS and EDX maps were acquired using the Nion microscope at 60 keV (for mapped regions, see fig. S35).

Simulation of conductive networks

The computational model begins with a resistive network of identical conductors of magnitude $g_{S2} = 1$. During each iteration of the simulation, one random conductor transitions from its current phase to the next phase with a certain probability, unless that conductor is already in the final MoO_3 phase. If it does not transition, then one of the adjacent sites is chosen and the transition check process is repeated. The probabilities represent the differing transition rates that occur between phases. Although the transition rates are experimentally unknown, the assumption that they progress, such that ($MoS_2 \rightarrow$ 2D-MoO_x)p_1 and (2D-$MoO_x \rightarrow MoO_3$)p_2, where p_1 and p_2 indicate relative conversion probabilities for each process and $p_2 > p_1$, is made. This relationship stems from the fact that the MoS_2 basal plane is chemically unreactive, but any defective nucleation sites will more likely facilitate chemical reactions once they are formed (*59*). The sheet conductance was then calculated using Kirchhoff's and Ohm's laws (section S5). The iterations were continued until all conductors were in the insulating MoO_3 phase. Iterations in the simulation are a proxy to the plasma exposure time, with a certain number of phase transitions (or iterations) per unit time. We note that the phase conversion was instant and did not reflect the crossover between conductance regimes on a localized scale but rather on the scale of the whole network.

SUPPLEMENTARY MATERIALS

Supplementary material for this article is available at http://advances.sciencemag.org/cgi/content/full/4/3/eaao5031/DC1

section S1. Electrical characterization of MoS_2 samples
section S2. Surface analysis and optical contrast change
section S3. Spectroscopy
section S4. Scanning/transmission electron microscopy
section S5. Simulation of conductive networks
fig. S1. Cross section of the plasma cleaner (*61*).
fig. S2. Optical micrographs of various MoS_2 devices after EBL processing.
fig. S3. Sketch of the experimental geometry.
fig. S4. V_{TH} consistency check: The electrical measurement has negligible effects on the transfer curve of the sample without plasma treatment, with the threshold voltage not affected by hysteresis at the used sweep rate of ~2 V/s.
fig. S5. Full data set of electrical measurements for samples of all thicknesses.

fig. S6. Full data set of mobilities derived for samples of all thicknesses over plasma exposure time.
fig. S7. Full data set of subthreshold swings derived for samples of all thicknesses over plasma exposure time.
fig. S8. The effect of keeping a plasma-tuned sample in SEM vacuum chamber overnight.
fig. S9. Optical micrographs of a few-layer flake exposed to pure Ar plasma for several minutes.
fig. S10. Effect of pure Ar plasma treatment on electrical properties.
fig. S11. AFM height maps of the flake discussed in the main manuscript after 0, 2, 6, and 8 s of plasma exposure (from top to bottom), with line profiles extracted from the marked edges.
fig. S12. Visible drop in optical contrast of a 4L MoS_2 flake after 28 s of plasma treatment visualized in the intensity drop of each individual RGB channel relative to the substrate.
fig. S13. SEM images of the sample treated for 28 s, showing small pit-like visible regions of dark contrast, as well as significant change to the material on the bottom edge of the flake.
fig. S14. Fits of the MoS_2 Raman peaks used to extract peak shifts in the 4L sample in the main manuscript.
fig. S15. PL spectroscopy of plasma-treated monolayer MoS_2.
fig. S16. PL lifetime mapping of monolayer MoS_2.
fig. S17. Thin area of MoS_2 contained in a poly(methyl methacrylate) stamp after transfer from substrate onto the TEM grid.
fig. S18. EDX spectroscopy of plasma-treated monolayer MoS_2.
fig. S19. EDX mapping of plasma-treated monolayer MoS_2.
fig. S20. EDX and EELS spectroscopy performed on plasma-treated samples in the AC-STEM.
fig. S21. XPS spectral region highlighting the small presence of S-O bonding at 6 s of treatment.
fig. S22. XPS spectra of the Mo 4p, Mo 4s and Si 2s regions over plasma treatment time.
fig. S23. HRTEM images (beam energy = 300 keV) of monolayer MoS_2 after plasma exposure for (from left) 0, 2, 5, 10, and 20 s.
fig. S24. HRTEM images (beam energy = 300 keV) of few-layer MoS_2 after plasma exposures for (from upper left reading to the right) 0, 4, 16, and 31 s.
fig. S25. STEM images (beam energy = 20 keV) of few-layer MoS_2 flakes taken in a SEM using a transmission detector.
fig. S26. High-angle annular dark-field (HAADF) STEM images (beam energy = 300 keV in FEI TITAN) of same samples as in fig. S21; plasma-treated for 16 s.
fig. S27. Medium-angle annular dark-field AC-STEM image (beam energy = 60 keV in Nion UltraSTEM 200) of pristine bilayer MoS_2 before any plasma treatment.
fig. S28. HAADF AC-STEM images (beam energy = 60 keV in Nion UltraSTEM 200) of few-layer MoS_2 plasma-treated for 6 s.
fig. S29. HAADF AC-STEM images (beam energy = 60 keV in Nion UltraSTEM 200) of few-layer MoS_2 plasma-treated for 8 s.
fig. S30. Simulation of bilayer MoS_2 with a peeled monolayer area and a perforated void carried out in QSTEM software.
fig. S31. Comparison between experimentally imaged void and simulated bilayer region with top layer removed.
fig. S32. Close-to-normal distributions of residuals from data fits seen in Fig. 4B of the main manuscript, confirming goodness of linear fit.
fig. S33. Histograms summarizing distribution of areas of etched pits after 6 and 8 s of plasma treatment.
fig. S34. Distribution of lateral sizes of voids after 8 s of etching.
fig. S35. Mapping regions scanned in the Nion UltraSTEM 200 at 60 keV for locally resolved spectroscopies of few-layer MoS_2.
fig. S36. Plot of concentration of the three phases in the simulation as they change with iteration number.
fig. S37. Trial-and-error plots for different combinations of conductances between the three phases C1, C2, and C3.
fig. S38. Comparison of simulated sheet conductance evolutions for schemes where sites are destroyed/not destroyed.
scheme S1. Cartoon of multilayer MoS_2 sample being oxidized by Ar/O_2 plasma from both sides when the sample is suspended on a TEM grid.
table S1. Peak shifts with exposure time for the Mo^{4+} 5/2 and Si 2s peaks relative to the C 1s core line, indicating that shifts are due to doping and not substrate charging.
References (*60*, *61*)

REFERENCES AND NOTES

1. B. Radisavljevic, A. Radenovic, J. Brivio, V. Giacometti, A. Kis, Single-layer MoS_2 transistors. *Nat. Nanotechnol.* **6**, 147–150 (2011).
2. B. Radisavljevic, A. Kis, Mobility engineering and a metal–insulator transition in monolayer MoS_2. *Nat. Mater.* **12**, 815–820 (2013).
3. D. Jariwala, V. K. Sangwan, L. J. Lauhon, T. J. Marks, M. C. Hersam, Emerging device applications for semiconducting two-dimensional transition metal dichalcogenides. *ACS Nano* **8**, 1102–1120 (2014).
4. D. Lembke, S. Bertolazzi, A. Kis, Single-layer MoS_2 electronics. *Acc. Chem. Res.* **48**, 100–110 (2015).
5. V. K. Sangwan, D. Jariwala, I. S. Kim, K.-S. Chen, T. J. Marks, L. J. Lauhon, M. C. Hersam, Gate-tunable memristive phenomena mediated by grain boundaries in single-layer MoS_2. *Nat. Nanotechnol.* **10**, 403–406 (2015).
6. Y.-C. Lin, D. O. Dumcenco, Y.-S. Huang, K. Suenaga, Atomic mechanism of the semiconducting-to-metallic phase transition in single-layered MoS_2. *Nat. Nanotechnol.* **9**, 391–396 (2014).
7. J. S. Kim, J. Kim, J. Zhao, S. Kim, J. H. Lee, Y. Jin, H. Choi, B. H. Moon, J. J. Bae, Y. H. Lee, S. C. Lim, Electrical transport properties of polymorphic MoS_2. *ACS Nano* **10**, 7500–7506 (2016).
8. D. S. Fox, Y. Zhou, P. Maguire, A. O'Neill, C. Ó'Coileáin, R. Gatensby, A. M. Glushenkov, T. Tao, G. S. Duesberg, I. V. Shvets, M. Abid, M. Abid, H.-C. Wu, Y. Chen, J. N. Coleman, J. F. Donegan, H. Zhang, Nanopatterning and electrical tuning of MoS_2 layers with a subnanometer helium ion beam. *Nano Lett.* **15**, 5307–5313 (2015).
9. P. Cheng, K. Sun, Y. H. Hu, Memristive behavior and ideal memristor of 1T phase MoS_2 nanosheets. *Nano Lett.* **16**, 572–576 (2016).
10. M. Chen, H. Nam, S. Wi, L. Ji, X. Ren, L. Bian, S. Lu, X. Liang, Stable few-layer MoS_2 rectifying diodes formed by plasma-assisted doping. *Appl. Phys. Lett.* **103**, 142110 (2013).
11. S. Wi, H. Kim, M. Chen, H. Nam, L. J. Guo, E. Meyhofer, X. Liang, Enhancement of photovoltaic response in multilayer MoS_2 induced by plasma doping. *ACS Nano* **8**, 5270–5281 (2014).
12. M. Chen, H. Nam, S. Wi, G. Priessnitz, I. M. Gunawan, X. Liang, Multibit data storage states formed in plasma-treated MoS_2 transistors. *ACS Nano* **8**, 4023–4032 (2014).
13. N.-Y. Cui, N. M. D. Brown, A. McKinley, An AFM study of the topography of natural MoS_2 following treatment in an RF–oxygen plasma. *Appl. Surf. Sci.* **151**, 17–28 (1999).
14. P. D. Fleischauer, Fundamental aspects of the electronic structure, materials properties and lubrication performance of sputtered MoS_2 films. *Thin Solid Films* **154**, 309–322 (1987).
15. J. B. Park, C. B. France, B. A. Parkinson, Scanning tunneling microscopy investigation of nanostructures produced by Ar^+ and He^+ bombardment of MoS_2 surfaces. *J. Vac. Sci. Technol. B Nanotechnol. Microelectron. Mater. Process. Meas. Phenom.* **23**, 1532–1542 (2005).
16. D. Kim, H. Du, T. Kim, S. Shin, S. Kim, M. Song, C. Lee, J. Lee, H. Cheong, D. H. Seo, S. Seo, The enhanced low resistance contacts and boosted mobility in two-dimensional p-type WSe_2 transistors through Ar^+ ion-beam generated surface defects. *AIP Adv.* **6**, 105307 (2016).
17. M. R. Islam, N. Kang, U. Bhanu, H. P. Paudel, M. Erementchouk, L. Tetard, M. N. Leuenberger, S. I. Khondaker, Tuning the electrical property *via* defect engineering of single layer MoS_2 by oxygen plasma. *Nanoscale* **6**, 10033–10039 (2014).
18. S. I. Khondaker, M. R. Islam, Bandgap engineering of MoS_2 flakes via oxygen plasma: A layer dependent study. *J. Phys. Chem. C* **120**, 13801–13806 (2016).
19. K.-C. Chen, C.-R. Wu, X.-R. Chang, S.-W. Chang, S.-C. Lee, S.-Y. Lin, Enhancement of field-effect mobility in molybdenum-disulfide transistor through the treatment of low-power oxygen plasma. *Jpn. J. Appl. Phys.* **55**, 090302 (2016).
20. W. Yang, Q.-Q. Sun, Y. Geng, L. Chen, P. Zhou, S.-J. Ding, D. W. Zhang, The integration of sub-10 nm gate oxide on MoS_2 with ultra low leakage and enhanced mobility. *Sci. Rep.* **5**, 11921 (2015).
21. H. Nan, Z. Wu, J. Jiang, A. Zafar, Y. You, Z. Ni, Improving the electrical performance of MoS_2 by mild oxygen plasma treatment. *J. Phys. D Appl. Phys.* **50**, 154001 (2017).
22. M.-Y. Ryu, H.-K. Jang, K. J. Lee, M. Piao, S.-P. Ko, M. Shin, J. Huh, G.-T. Kim, Triethanolamine doped multilayer MoS_2 field effect transistors. *Phys. Chem. Chem. Phys.* **19**, 13133–13139 (2017).
23. J. Guo, B. Yang, Z. Zheng, J. Jiang, Observation of abnormal mobility enhancement in multilayer MoS_2 transistor by synergy of ultraviolet illumination and ozone plasma treatment. *Physica E* **87**, 150–154 (2017).
24. W.-B. Zhang, Q. Qu, K. Lai, High-mobility transport anisotropy in few-layer MoO_3 and its origin. *ACS Appl. Mater. Interfaces* **9**, 1702–1709 (2017).
25. S. Balendhran, J. Deng, J. Z. Ou, S. Walia, J. Scott, J. Tang, K. L. Wang, M. R. Field, S. Russo, S. Zhuiykov, M. S. Strano, N. Medhekar, S. Sriram, M. Bhaskaran, K. Kalantar-Zadeh, Enhanced charge carrier mobility in two-dimensional high dielectric molybdenum oxide. *Adv. Mater.* **25**, 108 (2013).
26. M. M. Y. A. Alsaif, A. F. Chrimes, T. Daeneke, S. Balendhran, D. O. Bellisario, Y. Son, M. R. Field, W. Zhang, H. Nili, E. P. Nguyen, K. Latham, J. van Embden, M. S. Strano, J. Z. Ou, K. Kalantar-zadeh, High-performance field effect transistors using electronic inks of 2D molybdenum oxide nanoflakes. *Adv. Funct. Mater.* **26**, 91–100 (2016).
27. F. Giannazzo, G. Fisichella, G. Greco, S. Di Franco, I. Deretzis, A. La Magna, C. Bongiorno, G. Nicotra, C. Spinella, M. Scopelliti, B. Pignataro, S. Agnello, F. Roccaforte, Ambipolar MoS_2 transistors by nanoscale tailoring of Schottky barrier using oxygen plasma functionalization. *ACS Appl. Mater. Interfaces* **9**, 23164–23174 (2017).
28. R. Dhall, M. R. Neupane, D. Wickramaratne, M. Mecklenburg, Z. Li, C. Moore, R. K. Lake, S. Cronin, Direct bandgap transition in many-layer MoS_2 by plasma-induced layer decoupling. *Adv. Mater.* **27**, 1573–1578 (2015).
29. V. Buck, Lattice parameters of sputtered MoS_2 films. *Thin Solid Films* **198**, 157–167 (1991).
30. E. Schmidt, F. Weill, G. Meunier, A. Levasseur, New amorphous molybdenum oxysulfides obtained in the form of thin films and their characterization by TEM. *Thin Solid Films* **245**, 34–39 (1994).

31. J. R. Lince, $MoS_{2-x}O_x$ solid solutions in thin films produced by rf-sputter-deposition. *J. Mater. Res.* **5**, 218–222 (1990).
32. R. Rao, A. E. Islam, P. M. Campbell, E. M. Vogel, B. Maruyama, *In situ* thermal oxidation kinetics in few layer MoS_2. *2D Mater.* **4**, 025058 (2017).
33. T. Y. Ko, A. Jeong, W. Kim, J. Lee, Y. Kim, J. E. Lee, G. H. Ryu, K. Park, D. Kim, Z. Lee, M. H. Lee, C. Lee, S. Ryu, On-stack two-dimensional conversion of MoS_2 into MoO_3. *2D Mater.* **4**, 014003 (2017).
34. Y. Guo, J. Robertson, Origin of the high work function and high conductivity of MoO_3. *Appl. Phys. Lett.* **105**, 222110 (2014).
35. S. Y. Lee, U. J. Kim, J. Chung, H. Nam, H. Y. Jeong, G. H. Han, H. Kim, H. M. Oh, H. Lee, H. Kim, Y.-G. Roh, J. Kim, S. W. Hwang, Y. Park, Y. H. Lee, Large work function modulation of monolayer MoS_2 by ambient gases. *ACS Nano* **10**, 6100–6107 (2016).
36. T. N. Walter, F. Kwok, H. Simchi, H. M. Aldosari, S. E. Mohney, Oxidation and oxidative vapor-phase etching of few-layer MoS_2. *J. Vac. Sci. Technol. B Nanotechnol. Microelectron. Mater. Process. Meas. Phenom.* **35**, 021203 (2017).
37. N. Choudhary, M. R. Islam, N. Kang, L. Tetard, Y. Jung, S. I. Khondaker, Two-dimensional lateral heterojunction through bandgap engineering of MoS_2 via oxygen plasma. *J. Phys. Condens. Matter* **28**, 364002 (2016).
38. H. Zhu, X. Qin, L. Cheng, A. Azcatl, J. Kim, R. M. Wallace, Remote plasma oxidation and atomic layer etching of MoS_2. *ACS Appl. Mater. Interfaces* **8**, 19119–19126 (2016).
39. H. Li, Q. Zhang, C. C. R. Yap, B. K. Tay, T. H. T. Edwin, A. Olivier, D. Baillargeat, From bulk to monolayer MoS_2: Evolution of Raman scattering. *Adv. Funct. Mater.* **22**, 1385–1390 (2012).
40. C. Lee, H. Yan, L. E. Brus, T. F. Heinz, J. Hone, S. Ryu, Anomalous lattice vibrations of single- and few-layer MoS_2. *ACS Nano* **4**, 2695–2700 (2010).
41. N. Kang, H. P. Paudel, M. N. Leuenberger, L. Tetard, S. I. Khondaker, Photoluminescence quenching in single-layer MoS_2 via oxygen plasma treatment. *J. Phys. Chem. C* **118**, 21258–21263 (2014).
42. A. T. Neal, R. Pachter, S. Mou, P-type conduction in two-dimensional MoS_2 via oxygen incorporation. *Appl. Phys. Lett.* **110**, 193103 (2017).
43. D. O. Scanlon, G. W. Watson, D. J. Payne, G. R. Atkinson, R. G. Egdell, D. S. L. Law, Theoretical and experimental study of the electronic structures of MoO_3 and MoO_2. *J. Phys. Chem. C* **114**, 4636–4645 (2010).
44. P. J. Cumpson, The Thickogram: A method for easy film thickness measurement in XPS. *Surf. Interface Anal.* **29**, 403–406 (2000).
45. M. A. Baker, R. Gilmore, C. Lenardi, W. Gissler, XPS investigation of preferential sputtering of S from MoS_2 and determination of MoS_x stoichiometry from Mo and S peak positions. *Appl. Surf. Sci.* **150**, 255–262 (1999).
46. S. McDonnell, A. Azcatl, R. Addou, C. Gong, C. Battaglia, S. Chuang, K. Cho, A. Javey, R. M. Wallace, Hole contacts on transition metal dichalcogenides: Interface chemistry and band alignments. *ACS Nano* **8**, 6265–6272 (2014).
47. S. Chuang, C. Battaglia, A. Azcatl, S. McDonnell, J. S. Kang, X. Yin, M. Tosun, R. Kapadia, H. Fang, R. M. Wallace, A. Javey, MoS_2 P-type transistors and diodes enabled by high work function MoO_x contacts. *Nano Lett.* **14**, 1337–1342 (2014).
48. J. Yang, S. Kim, W. Choi, S. H. Park, Y. Jung, M.-H. Cho, H. Kim, Improved growth behavior of atomic-layer-deposited high-*k* dielectrics on multilayer MoS_2 by oxygen plasma pretreatment. *ACS Appl. Mater. Interfaces* **5**, 4739–4744 (2013).
49. L. Tao, X. Duan, C. Wang, X. Duan, S. Wang, Plasma-engineered MoS_2 thin-film as an efficient electrocatalyst for hydrogen evolution reaction. *Chem. Commun.* **51**, 7470–7473 (2015).
50. T. Saburi, H. Murata, T. Suzuki, Y. Fujii, K. Kiuchi, Oxygen plasma interactions with molybdenum: Formation of volatile molybdenum oxides. *J. Plasma Fusion Res.* **78**, 3–4 (2002).
51. W. S. Leong, Y. Li, X. Luo, C. T. Nai, S. Y. Quek, J. T. L. Thong, Tuning the threshold voltage of MoS_2 field-effect transistors *via* surface treatment. *Nanoscale* **7**, 10823–10831 (2015).
52. V. P. Zhdanov, nm-sized metal particles on a semiconductor surface, Schottky model, etc. *Surf. Sci.* **512**, L331–L334 (2002).
53. S. Das, J. Appenzeller, Where does the current flow in two-dimensional layered systems? *Nano Lett.* **13**, 3396–3402 (2013).
54. C. G. da Rocha, H. G. Manning, C. O'Callaghan, C. Ritter, A. T. Bellew, J. J. Boland, M. S. Ferreira, Ultimate conductivity performance in metallic nanowire networks. *Nanoscale* **7**, 13011–13016 (2015).
55. C. O'Callaghan, C. da Rocha, H. G. Manning, J. J. Boland, M. S. Ferreira, Effective medium theory for the conductivity of disordered metallic nanowire networks. *Phys. Chem. Chem. Phys.* **18**, 27564–27571 (2016).
56. J. A. Fairfield, C. G. Rocha, C. O'Callaghan, M. S. Ferreira, J. J. Boland, Co-percolation to tune conductive behaviour in dynamical metallic nanowire networks. *Nanoscale* **8**, 18516–18523 (2016).
57. T. Gebele, Site percolation threshold for square lattice. *J. Phys. A Math. Gen.* **17**, L51 (1984).
58. Y.-Q. Bie, Y.-B. Zhou, Z.-M. Liao, K. Yan, S. Liu, Q. Zhao, S. Kumar, H.-C. Wu, G. S. Duesberg, G. L. W. Cross, J. Xu, H. Peng, Z. Liu, D.-P. Yu, Site-specific transfer-printing of individual graphene microscale patterns to arbitrary surfaces. *Adv. Mater.* **23**, 3938–3943 (2011).
59. S. KC, R. C. Longo, R. M. Wallace, K. Cho, Surface oxidation energetics and kinetics on MoS_2 monolayer. *J. Appl. Phys.* **117**, 135301 (2015).
60. A. Ortiz-Conde, F. G. Sánchez, J. J. Liou, A. Cerdeira, M. Estrada, Y. Yue, A review of recent MOSFET threshold voltage extraction methods. *Microelectron. Reliab.* **42**, 583–596 (2002).
61. P. E. Fischione, J. Ringnada, Y. Feng, T. Krekels, M. Hayies, H. O. Colijn, M. J. Mills, J. M. Wiezorek, The use of a cold gas plasma for the final processing of contamination-free TEM specimens, in *Specimen Preparation for Transmission Electron Microscopy of Materials IV*, R. M. Anderson, S. D. Walck, Eds., (Materials Research Society Symposia Proceedings 480, 1997).

Acknowledgments: We are grateful to the staff at the Advanced Microscopy Laboratory, Centre for Research on Adaptive Nanostructures and Nanodevices (CRANN), Trinity College Dublin, for their continued technical support. We thank S. Callaghan for fruitful discussions regarding XPS. **Funding:** The work at the School of Physics and CRANN at Trinity College Dublin was supported by Science Foundation Ireland (grant nos. 11/PI/1105, 12/TIDA/I2433, 07/SK/I1220a, 12/IA/1482, and 08/CE/I1432) and the Irish Research Council (grant nos. GOIPG/2014/972, GOIPG/2013/680, and EPSPG/2011/239). C.P.C. and G.S.D. acknowledge support of Science Foundation Ireland under grant nos. 12/RC/2278 and 15/IA/3131. J.J.B. acknowledge support of European Research Council under grant no. 321160. **Author contributions:** J.J. analyzed the data, created the figures, and wrote the manuscript with input from C.O. and H.Z. I.O. discovered the phenomenon. J.J. and Y.Z. conducted subsequent plasma exposures and electrical tests. C.O. and E.W. carried out the resistor network modeling. Y.Z. performed monolayer Raman experiments, whereas C.P.C. and J.J. performed 4L Raman experiments. P.M. and J.J. carried out SEM imaging and EDX measurements. D.S.F. and J.J. performed HRTEM and STEM. C.D. acquired AC-STEM images and associated EELS and EDX maps. A.S. analyzed the AC-STEM results and performed QSTEM simulations. J.J., Y.Z., and J.J.G. carried out the monolayer PL measurements. C.P.C. and J.J. collected the 4L PL data. C.M. and J.J. performed XPS experiments and analysis. D.K. and J.J. carried out AFM experiments. M.S.F., G.S.D., A.L.B., J.J.B., V.N., and H.Z. oversaw the experimental work. H.Z. conceived the study and supervised the project. All authors have given approval for the final version of the manuscript. **Competing interests:** The authors declare that they have no competing interests. **Data and materials availability:** All data needed to evaluate the conclusions in the paper are present in the paper and/or the Supplementary Materials. Additional data related to this paper may be requested from H.Z. Raw data (code and source data for graphs) generated and/or analyzed during the current study are available in the Zenodo repository at: DOI:10.5281/zenodo.1160542.

Submitted 28 July 2017
Accepted 24 January 2018
Published 2 March 2018
10.1126/sciadv.aao5031

Citation: J. Jadwiszczak, C. O'Callaghan, Y. Zhou, D. S. Fox, E. Weitz, D. Keane, C. P. Cullen, I. O'Reilly, C. Downing, A. Shmeliov, P. Maguire, J. J. Gough, C. McGuinness, M. S. Ferreira, A. L. Bradley, J. J. Boland, G. S. Duesberg, V. Nicolosi, H. Zhang, Oxide-mediated recovery of field-effect mobility in plasma-treated MoS_2. *Sci. Adv.* **4**, eaao5031 (2018).

Science Advances

Oxide-mediated recovery of field-effect mobility in plasma-treated MoS_2

Jakub Jadwiszczak, Colin O'Callaghan, Yangbo Zhou, Daniel S. Fox, Eamonn Weitz, Darragh Keane, Conor P. Cullen, Ian O'Reilly, Clive Downing, Aleksey Shmeliov, Pierce Maguire, John J. Gough, Cormac McGuinness, Mauro S. Ferreira, A. Louise Bradley, John J. Boland, Georg S. Duesberg, Valeria Nicolosi and Hongzhou Zhang

Sci Adv **4** (3), eaao5031.
DOI: 10.1126/sciadv.aao5031